A Model for Intracellular Trafficking of Adenoviral Vectors

Anh-Tuan Dinh, Theo Theofanous, and Samir Mitragotri
Department of Chemical Engineering, University of California, Santa Barbara, California 93106

ABSTRACT Here we develop an integrative computational framework to model biophysical processes involved in viral gene delivery. The model combines reaction-diffusion-advection equations that describe intracellular trafficking with kinetic equations that describe transcription and translation of the exogenous DNA. It relates molecular-level trafficking events to whole-cell distribution of viruses. The approach makes use of the current understanding of cellular processes and data from single-particle single-cell imaging experiments. The model reveals two important parameters that characterize viral transport at the population level, namely, the effective velocity, V_{eff}, and the effective diffusion coefficient, D_{eff}. V_{eff} measures virus's net movement rate and D_{eff} represents the total dispersion rate. We employ the model to study the influence of microtubule-mediated movements on nuclear targeting and gene expression of adenoviruses of type 2 and type 5 in HeLa and A549 cells. Effects of microtubule organization and the presence of microtubule-destabilizing drugs on viral transport were analyzed and quantified. Model predictions agree well with experimental data available in literature. The paper serves as a guide for future theoretical and experimental efforts to understand viral gene delivery.

INTRODUCTION

Viruses have been used as gene delivery vehicles in a number of gene therapy studies (1). To successfully deliver DNA into the nucleus, viruses must facilitate cell-specific binding, internalization by endocytosis, escape from endocytic vesicles into the cytosol, transport in the cytoplasm, translocation across the nuclear envelope, and finally expression of the delivered gene. A quantitative understanding of these physical processes, especially in an integrated mode, is still lacking.

Advances in fluorescence microscopy (2,3) have allowed researchers to follow real-time movements of viruses inside living cells at the single-particle level. Useful data on intracellular transport and distribution of viruses have been obtained for various systems (4–6). For instance, adenoviruses (Ads), a popular viral gene vector, have been shown to utilize motor-assisted transport on microtubules for efficient nuclear targeting (6–8). Depolymerization of microtubules by nocodazole inhibited motor-assisted transport on microtubules (6) and reduced expression of the delivered DNA (9).

Relatively little attention has been paid to developing quantitative models of viral gene delivery. Previous pharmacokinetic models of virus infection (10–12) approximated all trafficking events, including transport-related steps, as kinetic processes, characterized by rate constants. This yields a number of ordinary differential equations to describe viral concentrations in different cellular compartments. Although kinetic models can effectively describe the ultimate outcome of gene delivery, that is, gene expression; a number of characteristic dynamic events, such as microtubule-dependent transport are not brought out due to imposition of transport processes on kinetic equations. Also, spatial organization of cells is not properly accounted for in kinetic models. Therefore, it is of interest to develop a new modeling approach that captures the inherent properties of viral dynamics and predicts viral behaviors that can be directly compared to data obtained from microscopic experiments.

Recently, Smith and Simmons (13) have developed a one-dimensional (1D) macroscopic model for motor-assisted transport of intracellular particles (vesicles, organelles, etc.) on a network of aligned filaments. The particles (complexes of vesicles and motor proteins) switch intermittently between distinct movement states, namely diffusion and directional transport on the filaments. This multistate description of particle motion relates the kinetics of particle-filament association and dissociation to the distribution of particles along the filaments. They examined the steady-state and transient solutions of unidirectional and symmetric bidirectional models. Two important apparent transport parameters that characterize long-term particle displacement were identified: drift velocity, V_{eff} and effective diffusion coefficient D_{eff}. D_{eff} represents the dispersion of particles within a frame of reference moving with a net velocity of V_{eff}. Both parameters depend on free-diffusion coefficient, velocity of motor-driven transport, and rates of particle binding to and detaching from filaments.

In this study, we integrate the above model of motor-assisted transport with several basic features of pharmacokinetic models to describe two-dimensional (2D) intracellular trafficking of viruses. In essence, we replace the lumped representation of microtubular transport and cytosolic diffusion in earlier models of gene delivery with transport theories. The remaining steps, for example, receptor-mediated binding, internalization, endosomal escape, and nuclear translocation are described using kinetic equations. The viruses are either bound to cell membrane, caged inside endosomes, free in cytosol, or bound to nuclear membrane. The

---

Submitted January 11, 2005, and accepted for publication June 13, 2005.

Address reprint requests to Samir Mitragotri, Dept. of Chemical Engineering, University of California, Santa Barbara, CA 93106. Tel.: 805-893-5774; Fax: 805-893-4731; E-mail: samir@engineering.ucsb.edu.

0006-3495/05/09/1574/15 $2.00

doi: 10.1529/biophysj.105.059477

viral species are defined according to these distinct biophysical states. Each species is characterized by a set of transport coefficients and a transition rate to the next state. As a result, we obtain a system of transport-reaction equations for concentrations of each viral species as a function of distance from the cell center. The equations were solved numerically using standard algorithms for partial differential equations (PDEs). This allowed us to determine the accumulation of viruses in the nuclear region. Transcription and translation of the exogenous DNA delivered by viruses were described by kinetic equations (14,15). Thus, the model presented here represents a complete description of viral gene delivery at the cellular level. Such models provide a platform to integrate existing experimental observations and qualitative hypotheses in a consistent manner.

The model is employed to study intracellular distribution and gene expression of subgroup C adenoviruses (Ad2 and Ad5) in A549 and HeLa cells. Transport coefficients are directly adapted from previous particle tracking experiments of Ads (6). Other model parameters are determined from past literature reports. Two sets of in vitro experiments were used to validate the model, namely, quantitative imaging experiments (16) and gene expression experiments (9). Model predictions agree well with both experimental data. A careful sensitivity analysis was performed to identify the parameters that control the propagation of viruses inside cells. We conclude that viral nuclear targeting is strongly influenced by the effective velocity and diffusivity of cytosolic viruses, a conclusion consistent with previous analysis (13). We also investigate the role of microtubule distribution and dynamics by relating these cell-specific properties to the rate of virus-microtubule association. We apply this approach to quantify viral trafficking in the presence of nocodazole (NOC), a microtubule-depolymerizing drug. The model successfully captures the dose-dependent inhibitory effect of nocodazole on nuclear accumulation and gene expression of Ads, as observed in experiments. Finally, the model is used to propose possible designs of synthetic gene delivery systems and new antiviral strategies.

MODEL FORMULATION

Physical description of the gene delivery pathway of adenoviruses

Adenoviruses are nonenveloped icosahedral particles ~90 nm in diameter (17). They replicate and produce progeny virions within the nucleus of infected cells. Adenoviruses are classified into six different serotypes (A–F). The subgroup C Ads, including Ad2 and Ad5, infect the upper airway and are also popular gene vectors (18). In this study, we focus on modeling intracellular transport of Ad2 and Ad5.

Intracellular trafficking of subgroup C Ad is schematically shown in Fig. 1 *a*. Viruses participate in a stepwise uncoating program (7). Upon internalization by receptor-mediated endocytosis, the viruses are delivered to endosomes, which exhibit bidirectional transport on microtubules (19–21). To avoid subsequent transfer to lysosomes for enzymatic degradation, the virus employs a low-pH triggering mechanism to disrupt the endosomal membrane, and escapes to the cytosol. To reach the nucleus effectively, the cytosolic virion utilizes the microtubule-based transport system (6–9). Once localized in the perinuclear region, the viral capsid docks at the nuclear pore complex in a process mediated by nuclear localization signal (22). This triggers the final disruption of the Ad2 virion (23), and release of the viral DNA genome into the cell nucleus. Ultimately, the viral DNA is transcribed, and gene products are synthesized.

Microtubules (MTs) are long filamentous polymers of the protein tubulin, with fast-growing plus-ends and slow-growing minus-ends (24). In most cells, MT minus-ends are anchored to the microtubule-organizing center (MTOC), located next to the nucleus, resulting in a uniform array of MTs (25). Cellular microtubules are highly dynamic. In vivo, they exhibit dynamic instability, i.e., stochastic switching between prolonged phases of assembly and rapid phases of disassembly. The frequency of transition from slow assembly to rapid disassembly (referred to as ''catastrophe'') determines the stability of the MT population (24). MT-based transport is mediated by molecular motors. Molecular motors are mechanochemical enzymes (ATPases) that convert chemical potential into mechanical energy. Most molecular motors move unidirectionally along a specific type of cytoskeletal tracks. Movements to the MT plus-ends (toward the cell periphery) require kinesins, whereas movements to the minus-ends (toward the cell nucleus) generally require cytoplasmic dyneins (8,26).

Under in vitro conditions, the cells under consideration (HeLa and A549) are nonpolarized and generally flat due to adhesion to a substrate. Cell thickness is often much smaller than the other dimensions. Viewing from the top, the cell interior is divided into two regions, cytoplasmic and nuclear, separated by the nuclear boundary. During experiments fluorescently labeled viruses have been found in the cytoplasmic as well as the nuclear region (16). However, because only viral DNA (and sometimes viral hexon protein) gets inside the nucleus (upon final disintegration of the viral capsid), the fluorescent particles seen in the nuclear region are in fact physically outside the nucleus. They appear in the region occupied by the nucleus due to projection from three to two dimensions. They could either be bound to the plasma membrane, inside the endosomes, free in the cytosol, or bound to the nuclear membrane depending on their stage of infection. They could also be fragments of disassembled capsids.

Another important property of the nuclear region is its deficiency or complete lack of microtubules, as seen in various visualizations of microtubule networks (6,27). Furthermore, high concentration of cellular organelles in the proximity of the nuclear membrane prevents viral particles from getting carried on microtubules effectively. Thus, it is

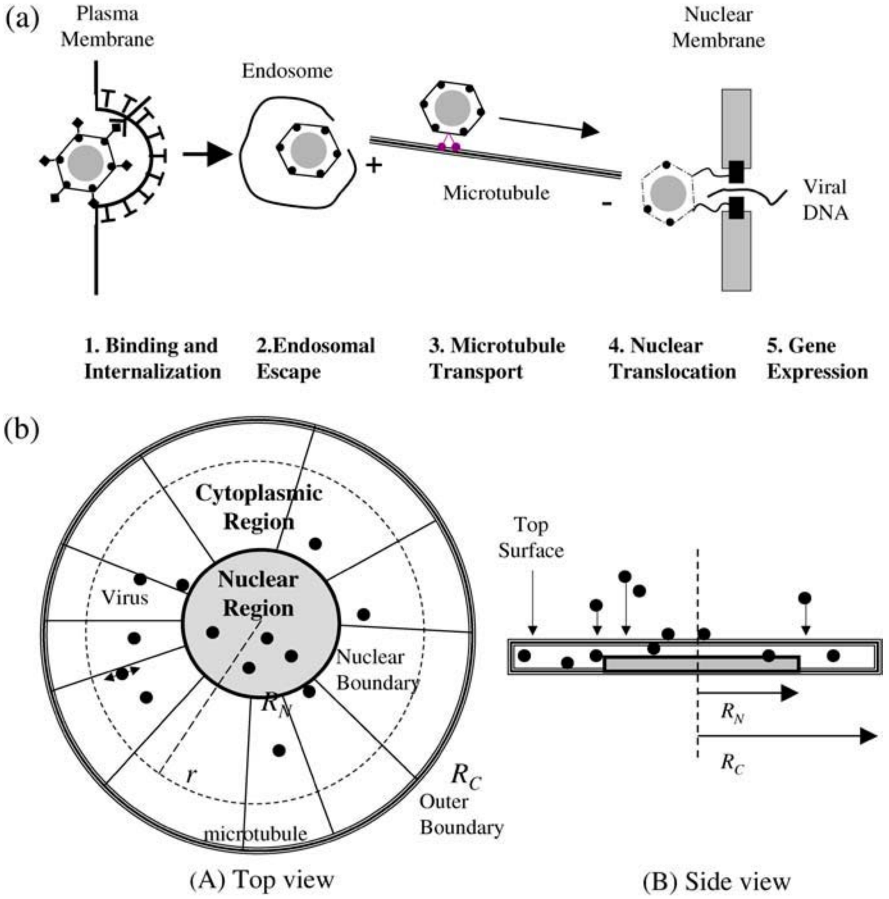

FIGURE 1 (*a*) Gene delivery pathway of subgroup C adenovirus, adapted from Meier and Greber (17). Ads are internalized by receptor-mediated endocytosis. Ads are then delivered to endosomes and escape to cytosol by a pH-mediated mechanism. They recruit motor proteins to boost microtubule-dependent viral transport toward the nucleus. Viruses then dock to nuclear pore complex and disassemble, releasing the viral DNA into the nucleus. (*b*) Schematic representation of a model cell. R_N and R_C are nuclear and cell radius, respectively; r is the distance to the cell center. Viruses enter the cell from the top. In the nuclear region ($r < R_N$), viruses can only diffuse. In the cytoplasmic region ($R_N < r < R_C$), viruses intermittently switch between diffusion and motor-assisted transport. As an approximation, we assume uniform concentration of endosomal and cytosolic viruses along the vertical direction.

believed that diffusion is the dominant, if not the only, transport mode in the nuclear region. On the contrary, viruses can participate in both diffusion and directional transport in the cytoplasmic region. The frequency of directional transport depends on complex interactions between motors, MTs and viral capsids.

Mathematical description of adenoviral gene delivery

As in single-particle tracking experiments, the proposed model follows the viral trajectory in a 2D domain. We employ a simplified two-dimensional abstraction of cells: a cell is represented by a circle of radius R_C with its nucleus occupying a circular region of radius R_N at the center (Fig. 1 *b*). This geometry imitates a cell spread on a surface. Viruses bind to and enter the cell from the top surface. MTs grow radially from the cell center toward the cell periphery, serving as cytoskeletal tracks for viral particles. To describe viral propagation within cells, we formulate a system of angular-averaged diffusion-advection-reaction equations for the viral density along the radial coordinate. For the translation and transcription of the exogenous DNA carried by viruses, we use a system of first-order kinetic equations. Definitions of variables and symbols are summarized in Table 1.

Intracellular trafficking

After binding to the cell membrane, the movement pathway of a viral particle can be characterized by five distinct biophysical states: i), membrane-bound virus (M), ii), endosomal virus (E), iii), cytosolic virus (C), iv), nuclear-bound virus (N), and v), disassembled viral capsids (cap). The states correspond to the stages of the gene delivery pathway described previously (Fig. 1 *a*). Transitions from one state to another depend on various biological and physical factors, such as location, interactions with cellular organelles, and viral uncoating.

In the cytoplasmic region ($R_N < r < R_C$), a viral particle can switch intermittently between diffusion and directional transport. To account for these distinct transport processes, we introduce transport state s, $s = \pm 1$ and 0 (0, diffusion; $+1$, plus-end directional transport; and -1, minus-end directional transport) as shown in Fig. 2. At a given point in time, each viral particle occupies one of the three transport states. In the nuclear region ($r < R_N$), the only transport state is diffusion as discussed in the previous section (s is always equal to 0). Note that the endosomal (E) and cytosolic (C) viruses can exist in the finite space between the plasma membrane and the nuclear envelope. The cytosolic viruses inside the nuclear region are the only species that can bind to the nuclear membrane, and participate in subsequent nuclear

TABLE 1 Nomenclature of mathematical symbols

$c_s^S(r, t)$	Areal density of particles at state S and substate s (no. of viruses per unit area)
$c(r, t)$	Areal density of particles at distance r from cell center
D_0	Free diffusion constant of the particle
D_{eff}^S	Effective diffusion coefficient for state S
DNA	Number of exogenous DNA entering the nucleus
δ_{MT}	Average spacing between microtubules
$f_{\pm}$	Fraction of actively transported particles in ± directions
f_{cat}	Frequency of catastrophe
$k_{\pm}$	Rates of binding of particles to microtubules
$k'_{\pm}$	Rates of detachment of particles from microtubules
$k_{\mathrm{bind}}/k_{\mathrm{unbind}}$	Rates of binding/detachment rates of viruses to/from cell membrane
$k_{\mathrm{disassembly}}$	Rates of capsid disintegration once virus is bound to nuclear membrane
$k_{\mathrm{transcription}}/k_{\mathrm{translation}}$	Rate of transcription and translation of viral DNA
$mRNA$	Number of transcripts
$n_s^S(r, t)$	Radial density of particles at state S and substate s at distance r from the cell center (no. of viruses per unit length)
$n(r, t)$	Radial density of particles at distance r from cell center
N_{MT}	Number of stable microtubules
P	Gene products
R	Distance from cell center
R_C, R_N	Radius of the outer boundary and the nuclear region
S, s	State and substate of viral particles
$V_{\pm}$	Average velocity of directional movements in ± direction
V_{eff}^S	Effective population velocity for state S
V_{ex}	Number of extracellular viruses per cell
v_0	Total number of viruses per cell
v_S	Total number of viruses at state S

translocation. We postulate that the rates of internalization and endosomal escape (number of events per second) are the same in both cytoplasmic and nuclear regions. Furthermore, we assume that MT-bound particles must detach from the MTs before participating in other physical processes. For instance, an endosomal virus must get off an MT before getting released into the cytosol.

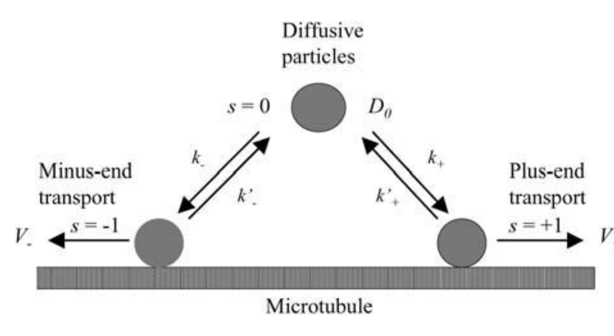

FIGURE 2 Transition map between transport states (0, diffusive transport; −1, minus-end transport; +1, plus-end transport); $k_{\pm}$ and $k'_{\pm}$ are binding/detachment rates to/from microtubules. $V_{\pm}$ are the velocities of motor-assisted transport in ± directions. D_0 is coefficient for free diffusion in cytosol.

Transitions between transport states of a viral particle are illustrated in Fig. 2. Following Smith and Simmons (13), we define V_+^S and V_-^S as velocities of directional movements toward the plus-end and the minus-end of microtubules; k_+^S, and k_-^S are first-order rate constants characterizing particle's transition from $s = 0$ to $s = +1$ and $s = -1$, respectively. $k_+^{\prime S}$ and $k_-^{\prime S}$ are the rate constants of the corresponding reverse processes. Thus, the cytoplasmic transport pattern of a viral species S is represented by seven parameters, D_0 (free diffusion coefficient), V_+^S, V_-^S, k_+^S, k_-^S, $k_+^{\prime S}$, and $k_-^{\prime S}$. An important postulation is that the state-dependent transport coefficients are independent of virus location inside the cytoplasmic region. Although data on spatial dependence of viral transport is not available, experimental observations in other systems seem to support this view. Quantifications of movements of PEI-DNA complexes in human fibroblast indicated that the parameters characterizing MT trafficking of these complexes are independent of spatial location (C. Pangarkar, unpublished data). Rodionov et al. (28) also arrived at a similar conclusion for transport of pigment granules in fish melanophores.

Because transport of viruses along the microtubules is essentially one-dimensional, a natural spatial coordinate for the problem is the distance from the cell center, r. Based on the proposed multistate description of transport, we formulate a system of macroscopic mass conservation equations for the viral species along the radial coordinate, averaging over all angles. The equations (Eqs. 1a–1e) are summarized in Table 2. The basic variable is the radial density $n_s^S(r, t)$ (number of viruses per length), which represents the number of viral particles at state S ($S = M, E, C, N$, and cap) and substate s (0, −1, and +1), at a distance r from the cell center. Note that $n_s^S(r, t)$ is not a local quantity but represents an ensemble average of particle positions with respect to the cell center, sampled over a large number of particles and a large population of cells. We choose to deal with the radial density because it conveniently captures the 1D nature of transport along the MTs. Alternatively, we can formulate the equations in term of the areal density $c_s^S(r, t)$. For comparison to experiments, we will convert $n(r, t)$ to $c(r, t)$. By employing this description, we are able to approximate a complex, three-dimensional transport phenomenon with a system of one-dimensional partial differential equations. This approach also enables us to properly describe two-dimensional diffusion of viral particles in the cytoplasm.

The total number of viruses at state S ($S = M, E, C$, or cap) is

$$v^S = \int_0^{R_C} n^S \, dr = \int_0^{R_C} (n_0^S + n_{+1}^S + n_{-1}^S) dr. \qquad (2)$$

Gene expression

The number of viruses bound to the nuclear membrane as a function of time is given by Eq. 1d. A reasonable assumption

TABLE 2 Governing equations for intracellular trafficking of viral particles

Biophysical state	Diffusion-advection-reaction equations
Membrane-bound (Eq. 1a)	$\frac{\partial n^{\mathrm{M}}}{\partial t} = D^{\mathrm{M}}\frac{\partial}{\partial r}\left[r\frac{\partial}{\partial r}\left(\frac{n^{\mathrm{M}}}{r}\right)\right] - k_{\mathrm{int}}n^{\mathrm{M}} + k_{\mathrm{bind}}\frac{2V_{\mathrm{ex}}r}{R_{\mathrm{C}}^{2}} - k_{\mathrm{unbind}}n_{\mathrm{M}}.$
Endosomal (Eq. 1b)	a), $R_{\mathrm{N}} < r < R_{\mathrm{C}}$ $\frac{\partial n_{0}^{\mathrm{E}}}{\partial t} = (k_{-}^{'\mathrm{E}}n_{-1}^{\mathrm{E}} + k_{+}^{'\mathrm{E}}n_{+1}^{\mathrm{E}}) - (k_{-}^{\mathrm{E}}n_{0}^{\mathrm{E}} + k_{+}^{\mathrm{E}}n_{0}^{\mathrm{E}}) + D^{\mathrm{E}}\frac{\partial}{\partial r}\left[r\frac{\partial}{\partial r}\left(\frac{n_{0}^{\mathrm{E}}}{r}\right)\right] + k_{\mathrm{int}}n^{\mathrm{M}} - k_{\mathrm{escape}}n_{0}^{\mathrm{E}}$ $\frac{\partial n_{-1}^{\mathrm{E}}}{\partial t} = -k_{-}^{'\mathrm{E}}n_{-1}^{\mathrm{E}} + k_{-}^{\mathrm{E}}n_{0}^{\mathrm{E}} - V_{-}^{\mathrm{E}}\frac{\partial n_{-1}^{\mathrm{E}}}{\partial r}$ $\frac{\partial n_{+1}^{\mathrm{E}}}{\partial t} = -k_{+}^{'\mathrm{E}}n_{+1}^{\mathrm{E}} + k_{+}^{\mathrm{E}}n_{0}^{\mathrm{E}} - V_{+}^{\mathrm{E}}\frac{\partial n_{+1}^{\mathrm{E}}}{\partial r}.$ b), $r < R_{\mathrm{N}}$ $\frac{\partial n_{0}^{\mathrm{E}}}{\partial t} = D^{\mathrm{E}}\frac{\partial}{\partial r}\left[r\frac{\partial}{\partial r}\left(\frac{n_{0}^{\mathrm{E}}}{r}\right)\right] + k_{\mathrm{int}}n^{\mathrm{M}} - k_{\mathrm{escape}}n_{0}^{\mathrm{E}}.$
Cytoplasmic (Eq. 1c)	a), $R_{\mathrm{N}} < r < R_{\mathrm{C}}$ $\frac{\partial n_{0}^{\mathrm{C}}}{\partial t} = (k_{-}^{'\mathrm{C}}n_{-1}^{\mathrm{C}} + k_{+}^{'\mathrm{C}}n_{+1}^{\mathrm{C}}) - (k_{-}^{\mathrm{C}}n_{0}^{\mathrm{C}} + k_{+}^{\mathrm{C}}n_{0}^{\mathrm{C}}) + D^{\mathrm{C}}\frac{\partial}{\partial r}\left[r\frac{\partial}{\partial r}\left(\frac{n_{0}^{\mathrm{C}}}{r}\right)\right] + k_{\mathrm{escape}}n_{0}^{\mathrm{E}}$ $\frac{\partial n_{-1}^{\mathrm{C}}}{\partial t} = -k_{-}^{'\mathrm{C}}n_{-\mathrm{C}}^{\mathrm{C}} + k_{-}^{\mathrm{C}}n_{0}^{\mathrm{C}} - V_{-}^{\mathrm{C}}\frac{\partial n_{-1}^{\mathrm{C}}}{\partial r}$ $\frac{\partial n_{+1}^{\mathrm{C}}}{\partial t} = -k_{+}^{'\mathrm{C}}n_{+\mathrm{C}}^{\mathrm{C}} + k_{+}^{\mathrm{C}}n_{0}^{\mathrm{C}} - V_{+}^{\mathrm{C}}\frac{\partial n_{+1}^{\mathrm{C}}}{\partial r}.$ b), $r < R_{\mathrm{N}}$ $\frac{\partial n_{0}^{\mathrm{C}}}{\partial t} = D^{\mathrm{C}}\frac{\partial}{\partial r}\left[r\frac{\partial}{\partial r}\left(\frac{n_{0}^{\mathrm{C}}}{r}\right)\right] + k_{\mathrm{escape}}n^{\mathrm{E}} - k_{\mathrm{nuclear}}n_{0}^{\mathrm{C}}.$
Nuclear-bound (Eq. 1d)	a), $R_{\mathrm{N}} < r < R_{\mathrm{C}}$ $n^{\mathrm{N}} = 0.$ b), $r < R_{\mathrm{N}}$ $\frac{\partial n^{\mathrm{N}}}{\partial t} = D^{\mathrm{N}}\frac{\partial}{\partial r}\left[r\frac{\partial}{\partial r}\left(\frac{n_{0}^{\mathrm{N}}}{r}\right)\right] - k_{\mathrm{disassembly}}n^{\mathrm{N}} + k_{\mathrm{nuclear}}n_{0}^{\mathrm{C}}.$
Empty capsid (Eq. 1e)	a), $R_{\mathrm{N}} < r < R_{\mathrm{C}}$ $\frac{\partial n_{0}^{\mathrm{cap}}}{\partial t} = (k_{-}^{'\mathrm{cap}}n_{-1}^{\mathrm{cap}} + k_{+}^{'\mathrm{Cap}}n_{+1}^{\mathrm{cap}}) - (k_{-}^{\mathrm{cap}}n_{0}^{\mathrm{cap}} + k_{+}^{\mathrm{cap}}n_{0}^{\mathrm{cap}}) + D^{\mathrm{cap}}\frac{\partial}{\partial r}\left[r\frac{\partial}{\partial r}\left(\frac{n_{0}^{\mathrm{cap}}}{r}\right)\right]$ $\frac{\partial n_{-1}^{\mathrm{cap}}}{\partial t} = -k_{-}^{'\mathrm{cap}}n_{-\mathrm{cap}}^{\mathrm{cap}} + k_{-}^{\mathrm{cap}}n_{\mathrm{cap0}}^{\mathrm{cap}} - V_{-}^{\mathrm{cap}}\frac{\partial n_{-1}^{\mathrm{cap}}}{\partial r}$ $\frac{\partial n_{+1}^{\mathrm{cap}}}{\partial t} = -k_{+}^{'\mathrm{cap}}n_{+\mathrm{C}}^{\mathrm{cap}} + k_{+}^{\mathrm{cap}}n_{0}^{\mathrm{cap}} - V_{+}^{\mathrm{cap}}\frac{\partial n_{+1}^{\mathrm{cap}}}{\partial r}.$ b), $r < R_{\mathrm{N}}$ $\frac{\partial n_{0}^{\mathrm{cap}}}{\partial t} = D^{\mathrm{cap}}\frac{\partial}{\partial r}\left[r\frac{\partial}{\partial r}\left(\frac{n_{0}^{\mathrm{cap}}}{r}\right)\right] + k_{\mathrm{disassembly}}n^{\mathrm{N}}.$

For definitions of the symbols, please refer to Table 1.

is that the amount of exogenous DNA entering the nucleus is proportional to the number of nuclear-bound viruses that disassemble. The equation for the evolution of exogenous DNA inside the nucleus is as follows:

$$\frac{dDNA}{dt} = \kappa_{\mathrm{DNA}} \int_0^{R_N} k_{\mathrm{dissasembly}} n^{\mathrm{N}} dr - k_{\mathrm{el\text{-}DNA}} DNA, \quad (3)$$

where κ_{DNA} is a proportionality constant, and $k_{\mathrm{el\text{-}DNA}}$ is the elimination rate of exogenous DNAs due to nuclease-mediated degradation and cell division.

The transcription and translation of exogenous DNA involves thousands of complex chemical reactions. In the simplest model of gene expression, mRNA is synthesized from DNA and protein is synthesized from mRNA (14). The ordinary differential equations that determine the temporal evolution of number of mRNA molecules, *mRNA,* and protein molecules, *P*, are

$$\frac{dmRNA}{dt} = k_{\mathrm{transcription}} DNA - k_{\mathrm{deg,mRNA}} mRNA \quad (4)$$

$$\frac{dP}{dt} = k_{\mathrm{translation}} mRNA - k_{\mathrm{deg,protein}} P, \quad (5)$$

where $k_{\mathrm{transcription}}$ and $k_{\mathrm{translation}}$ are the transcription and translation rate constants; $k_{\mathrm{deg,mRNA}}$ and $k_{\mathrm{deg,protein}}$ are the decay constants associated with the half-life of mRNA and proteins.

Boundary and initial conditions

The above system of ordinary differential equations and PDEs is accompanied by boundary and initial conditions. Axial symmetry and impermeable wall boundary conditions are applied at $r = 0$ and $r = R_C$, respectively.

The initial conditions depend on the experimental setup, which determines the allocation of viruses before internalization. In experiments using quantitative fluorescence microscopy, viruses in the extracellular solution were removed to provide a better quantification of viral distribution. First, cells and viruses were kept at low temperature to inhibit endocytosis. Then, unbound viruses were washed out and cells were incubated at physiological temperature for indicated amounts of time (16). Thus, initially, there are no extracellular viruses ($v_{\mathrm{ex}} = 0$) and all viruses are bound to cell membrane. Assuming that the probability of virus binding to any location on the cell surface is equal, the radial density of membrane-bound viruses at $t = 0$ is $n^{\mathrm{M}}(r) = n_0 = v_0 2r/R_C{}^2$ (v_0 is the total number of viruses per cell). The radial densities of other viral species are set to zero.

In the experiments measuring gene expression, viruses are added to the extracellular solution and incubated together with the cells at physiological condition. Then, the cells are lysed and assayed for gene expression activity and protein content (9). Thus, initially, all viruses are in the extracellular solution: $v_{\mathrm{ex}} = v_0$ and $n^{\mathrm{S}}(r) = 0$ ($S = M, E, C, N$, and cap). The depletion of extracellular viruses due to binding to cell membrane is described as follows (assuming the endocytic pathway is not saturated):

$$\frac{dv^{\mathrm{ex}}}{dt} = -k_{\mathrm{bind}} v^{\mathrm{ex}} + k_{\mathrm{unbind}} v^{\mathrm{M}}. \quad (6)$$

The total number of membrane-bound viruses, v^{M}, is related to membrane-bound radial density, n^{M}, by Eq. 2.

Numerical solution

The equations formulated above are solved numerically using second-order upwind scheme for spatial discretization of the PDEs and an explicit Euler scheme for time integration. The numerical algorithms were implemented in Matlab (The Mathworks, Natick, MA). To ensure numerical accuracy, we use small time step $\Delta t = 0.2$ s and grid size, $\Delta r = 0.1$ μm; Δt and Δr are much smaller than the characteristic length- and timescales of transport. They also must satisfy the Courant-Friedrichs-Lewy condition, $V\Delta t/\Delta r < 1$. The numerical solutions converge as we vary Δt from 0.05 to 2 s and Δr from 0.02 to 0.2 μm.

Model parameters

The parameters that characterize the transport properties of Ad2 viral particles in HeLa cells are summarized in Table 3. The parameter values were deduced from particle-tracking data (6). Other model parameters are determined from a variety of sources, and classified into three groups: two parameters describing cell geometry, four parameters describing transition between physical states, and four parameters describing protein synthesis (Table 4). Another important assumption is that all model parameters are independent of the ratio between the concentrations of cells and viruses. Appendix A provides further details of parameter estimation.

RESULTS

Spatiotemporal distribution of viral particles

The model was used to simulate intracellular trafficking of adenovirus type 2 (Ad2) in HeLa cells. The calculated areal density $c(r,t)$ is shown in Fig. 3 *a*. The areal density, which represents the number of viruses per unit area at a distance r from the center, is related to the radial density by $c(r,t) = n(r,t)/2\pi r$. It is normalized with $c_0 = v_0/\pi R_C^2$. At $t = 0$, the

TABLE 3 Transport coefficients in cytoplasm for different state of Ad2 in HeLa cells

Viral biophysical state	f_+	f_-	V_+ (μm/s)	V_- (μm/s)
Membrane-bound	5.4%	5.4%	0.11	−0.11
Endosomal	41.9%	35.5%	0.39	−0.36
Cytosolic	25.5%	33.1%	0.33	−0.31
Disassembled capsids	25.5%	33.1%	0.33	−0.31

Parameters are adapted from (6).

TABLE 4 Model parameters used for simulations of intracellular transport and gene expression of adenoviruses in HeLa cells

Parameter	Definition	Reference	Value
Cell geometry			
R_C	Mean membrane radius	(16)	21 μm
R_N	Mean nuclear radius	(16)	8.5 μm
Transition rates			
k_{int}	Rate of internalization	(41)	$1.2\ 10^{-3}\ s^{-1}$
k_{escape}	Rate of endosomal escape	(41)	$7.7\ 10^{-4} s^{-1}$
$k_{nuclear}$	Rate of binding to nuclear membrane	(7)	$4.8\ 10^{-4} s^{-1}$
$k_{disassembly}$	Rate of viral capsid disassembly	(7,23)	$9.6\ 10^{-5} s^{-1}$
Gene expression			
$k_{transcription}$	Transcription rate	(15)	$5.5\ 10^{-4}\ s^{-1}$
$k_{translation}$	Translation rate	(45)	$2.8\ 10^{-4}\ s^{-1}$
$k_{deg\text{-}mRNA}$	Elimination rate of mRNA	(46)	$3.8\ 10^{-5}\ s^{-1}$
$k_{deg\text{-}protein}$	Elimination rate of protein	(47)	$1.4\ 10^{-5}\ s^{-1}$

surface-bound viruses are uniformly distributed over the cell surface, hence, $c(r,t)$ is constant. Due to microtubule-dependent transport, viruses at the cell periphery are delivered to the nuclear region ($r/R_C < 0.4$). Fig.3 *a* displays a remarkable increase in the nuclear concentration at $t =$ 60–120 min postinternalization (p.i.). We also note that the density profiles in the cytoplasmic region at $t = 60$ min and $t = 120$ min display similar shapes. This suggests that the redistribution of viral particles due to microtubule-mediated transport in the cytoplasm has reached a quasiequilibrium state at $t \sim$ 30–60 min.

The predicted temporal evolution of the fraction of viruses at different biophysical states is depicted in Fig. 3 *b*. Initially, the number of endosomal and cytosol virions rise as the membrane-bound viruses are internalized by endocytosis. The number of endosomal virions peaks at 10 min. At 60 min p.i., ~95% of viruses have escaped from endosomes. The number of cytosolic viral particles rises sharply, reaching a maximum value at $t \sim 65$ min. Then, from ~1 to 4 h, the number of cytosolic viral particles declines as they are transported to the nuclear region and bind to the nuclear membrane. At $t = 120$ min, ~25% of internalized adenoviruses are bound to the nuclear membrane, and ~20% of viral capsids disintegrate, releasing the viral genome into the nucleus. Electron microscopic studies of herpes simplex virus in Vero cells showed similar time courses for endosomal, cytosolic, and empty capsids (29).

The simulation results are compared to the intracellular distribution data independently reported by Nakano and Greber (16). In these experiments, the intracellular domain is divided into four separate areas, namely, peripheral, cytoplasmic, perinuclear, and nuclear. The authors operationally defined the cell periphery as a 3.5-μm-wide ribbon and the nuclear periphery as a 1.8-μm-wide region extending 0.9 μm from both sides of the nuclear boundary. The fluorescence intensity, which is proportional to the number of viruses, was quantified for each area.

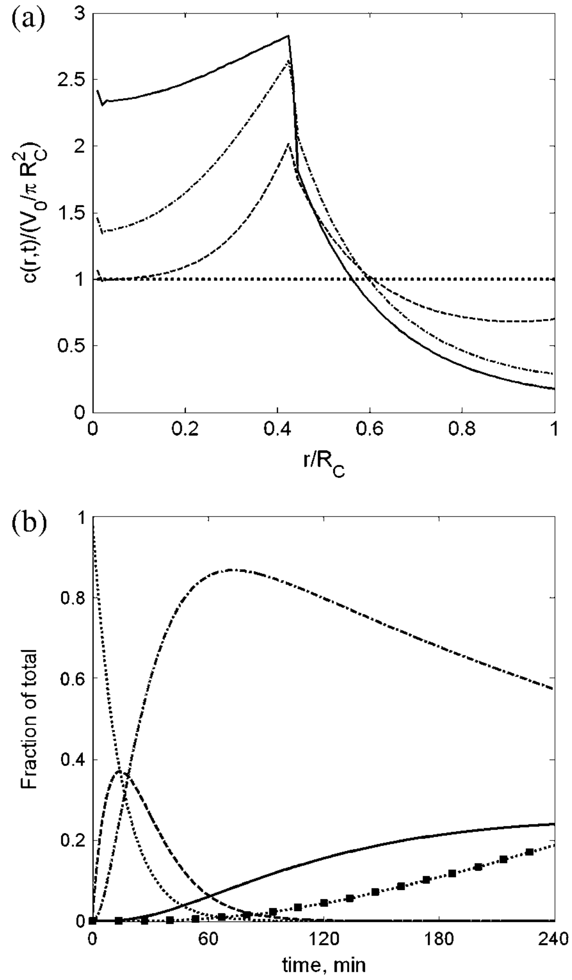

FIGURE 3 (*a*) Distribution of the normalized areal density, $c(r,t)/(v_0/\pi R_C^2)$, of adenoviruses in HeLa cells at $t = 0$min (*dotted line*), 30 min (*dashed line*), 60 min (*dot-dashed line*), and 120 min (*solid line*). The nuclear membrane is located at $R_N/R_C \sim 0.4$ ($R_N = 8.5$ μm, $R_C = 21$ μm). (*b*) Temporal evolution of fractions of viruses bound to membrane (M) (*dotted line*), inside endosomes (E) (*dashed line*), free in cytosol (C) (*dot-dashed line*), bound to nuclear membrane (N) (*solid line*), and fragmented capsids (cap) (*square-dotted line*).

Based on the results shown in Fig. 3 *a*, we calculate the average viral density, *c*, in each area as defined above and compare with the measured fluorescence signal. Without any fitted parameters, the model predicts the experimental data with good agreement (Fig. 4). The lines and the symbols correspond to model predictions and experimental data, respectively. At $t = 0$, the viruses in experimental data are not equally distributed on the cell membrane as postulated by the model, but slightly concentrated in the perinuclear and nuclear areas, possibly due to nonplanar topology of the membrane in the proximity of the nucleus. The viral density in the cell periphery declines between 0 and 30 min p.i, while the number of viruses in the cytoplasmic region remains relatively constant for a long

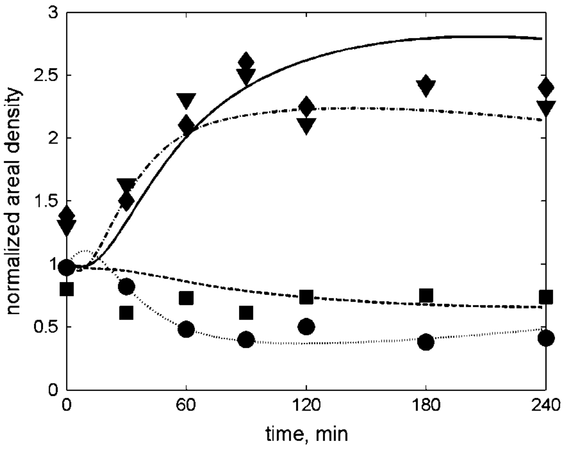

FIGURE 4 Distribution of Ad2s in HeLa cells for four different cellular areas: periphery (*dotted line*, model; ●, data), cytoplasm (*dashed line*, model; ■, data), perinuclear (*dash-dot line*, model; ◆, data), and nuclear (*solid line*, model; ▼, data). Data was reproduced from Nakano and Greber (16).

period of time. The fraction of viral particles present in the nuclear region doubles from ~25% initially to 60% at $t = 120$ min. Also, a significant portion of empty capsids are transported back to the cell periphery, resulting in an increase in viral concentrations in the cytoplasmic and peripheral regions. In the following section, we attempt to identify the parameters or groups of parameters that control the spatial spread of viruses inside cells.

Apparent transport coefficients

Microtubules can transport Ads while they are encapsulated in endosomes (19–21) and when they are released into the cytosol. However, as seen in Fig. 3 *b*, Ads only spend a brief period staying inside the endosomes. Thus, at long times, intracellular allocation of viral particles is primarily determined by movements of cytosolic viruses. The directionality of these movements is measured by the effective population velocity, $V_{\mathrm{eff}}^{\mathrm{C}}$, defined as follows (13):

$$V_{\mathrm{eff}}^{\mathrm{C}} = \frac{K_{+}^{\mathrm{C}} V_{+}^{\mathrm{C}} + K_{-}^{\mathrm{C}} V_{-}^{\mathrm{C}}}{K_{+}^{\mathrm{C}} + K_{-}^{\mathrm{C}} + 1} \cong f_{+}^{\mathrm{C}} V_{+}^{\mathrm{C}} + f_{-}^{\mathrm{C}} V_{-}^{\mathrm{C}}, \tag{7}$$

where $K_{\pm}^{\mathrm{C}} = (k_{\pm}^{\mathrm{C}} / k_{\pm}^{\prime \mathrm{C}})$, and $f_{\pm}^{\mathrm{C}}$ are the fractions of actively transported particles (see Appendix A). For Ad2 in HeLa cells (6), $V_{\mathrm{eff}}^{\mathrm{C}} = -0.019$ μm/s as determined from model parameters. Thus, on average, naked Ad2 particles in cytosol move preferentially toward the nucleus with a rate of 0.019 μm/s. Increase in the absolute value of V_{-}^{C} results in a faster rate of accumulation and a higher concentration of viruses in the nuclear area.

With an average absolute velocity of 0.019 μm/s, it would take a particle ~12 min to traverse the cytosol. It is reasonable to expect that all viruses would accumulate in the perinuclear and nuclear areas on the same timescale. However, as seen in Figs. 3 *a* and 4, there is a significant fraction of viruses in the cytoplasm and the periphery between 60 and 240 min. There must be a counteracting mechanism that prevents viruses from collecting at cell center. To explain this observation, we note that bidirectional random walks of cytosolic viruses also give rise to a form of facilitated diffusion along the radial coordinate. The effective diffusion coefficient that characterizes this process can be estimated as follows (13):

$$\begin{aligned} D_{\mathrm{eff}}^{\mathrm{C}} &= \frac{D_0 + K_{+}^{\mathrm{C}} (V_{+}^{\mathrm{C}} - V_{\mathrm{eff}}^{\mathrm{C}})^2 / k_{+}^{\prime} + K_{-}^{\mathrm{C}} (V_{-}^{\mathrm{C}} - V_{\mathrm{eff}}^{\mathrm{C}})^2 / k_{-}^{\prime}}{K_{+}^{\mathrm{C}} + K_{-}^{\mathrm{C}} + 1} \\ &\cong f_{+}^{\mathrm{C}} \frac{(V_{+}^{\mathrm{C}} - V_{\mathrm{eff}}^{\mathrm{C}})^2}{k_{+}^{\prime}} + f_{-}^{\mathrm{C}} \frac{(V_{-}^{\mathrm{C}} - V_{\mathrm{eff}}^{\mathrm{C}})^2}{k_{-}^{\prime}}. \end{aligned} \tag{8}$$

The effective diffusion rate represents the dispersion of virus particles in the frame of reference moving with velocity $V_{\mathrm{eff}}^{\mathrm{C}}$. Interestingly, $D_{\mathrm{eff}}^{\mathrm{C}}$ depends quadratically on the differences between $V_{\pm}^{\mathrm{C}}$ and $V_{\mathrm{eff}}^{\mathrm{C}}$. For Ad2 in HeLa cells (6), $D_{\mathrm{eff}}^{\mathrm{C}} \sim 0.12$ μm^2/s as determined from model parameters, which is two order-of-magnitudes larger than free diffusion coefficient. At long times, this leads to a gradual equilibration of viral concentration, n^{C}, along the radial coordinate. If $V_{\mathrm{eff}}^{\mathrm{C}} = 0$, we would expect a uniform distribution of n^{C} as function of r for $R_{\mathrm{N}} < r < R_{\mathrm{C}}$. For $V_{\mathrm{eff}}^{\mathrm{C}} \neq 0$, the quasi-steady-state distribution of cytosolic particles in the cytoplasmic region is established as a result of the interplay between $V_{\mathrm{eff}}^{\mathrm{C}}$ and $D_{\mathrm{eff}}^{\mathrm{C}}$.

$V_{\mathrm{eff}}^{\mathrm{C}}$ and $D_{\mathrm{eff}}^{\mathrm{C}}$ are, however, not independent of each other. Variations in one of the transport coefficients will affect both $V_{\mathrm{eff}}^{\mathrm{C}}$ and $D_{\mathrm{eff}}^{\mathrm{C}}$. To further examine the interdependency between $V_{\mathrm{eff}}^{\mathrm{C}}$ and $D_{\mathrm{eff}}^{\mathrm{C}}$, we vary the unbinding rate $k^{\prime \mathrm{C}}$ ($k^{\prime \mathrm{C}} = k_{-}^{\prime \mathrm{C}} = k_{+}^{\prime \mathrm{C}}$). The binding rate k^{C} is adjusted accordingly to maintain and the fractions of actively transported particles, f_{+}^{C}, and f_{-}^{C}, constant. This alters $D_{\mathrm{eff}}^{\mathrm{C}}$ but keeps $V_{\mathrm{eff}}^{\mathrm{C}}$ the same. For $V_{\mathrm{eff}}^{\mathrm{C}} = -0.019$ μm/s, we observe a considerable decline in nuclear concentration, as we decrease $k_{\mathrm{C}}^{\prime}$ from 10 to 0.1 s^{-1} and consequently increase in $D_{\mathrm{eff}}^{\mathrm{C}}$ from 0.008 to 0.6 μm^2/s (Fig. 5). For Ad2, $k_{\mathrm{C}}^{\prime}$ is ~0.5–1 s^{-1} (6). For a large value of $D_{\mathrm{eff}}^{\mathrm{C}}$, the nuclear density approaches 1.8. Similar observations were made for $V_{\mathrm{eff}}^{\mathrm{C}} = -0.01$ and -0.03 μm/s. In conclusion, $V_{\mathrm{eff}}^{\mathrm{C}}$ and $D_{\mathrm{eff}}^{\mathrm{C}}$ are two important parameters that determine the overall efficiency of nuclear-directed transport. The dependence of nuclear accumulation on $V_{\mathrm{eff}}^{\mathrm{C}}$ and $D_{\mathrm{eff}}^{\mathrm{C}}$ is not monotonic (see Discussion).

Effects of nocodazole

The frequency of directional movements on microtubules is strongly influenced by microtubule distribution and polymerization dynamics. As shown in Appendix B, the rate at which particles bind to and get carried on a microtubule (k) depends on the half-life of microtubules, $t_{1/2}^{\mathrm{MT}}$, and the average distance between two neighboring MTs, δ_{MT}. The half-life of microtubules signifies the stability of the cytoskeletal tracks and is inversely proportional to the rate of catastrophe, f_{cat}. If $t_{1/2}^{\mathrm{MT}}$ is short, particles might not be able to associate with an MT, before it disappears. δ_{MT} represents microtubule

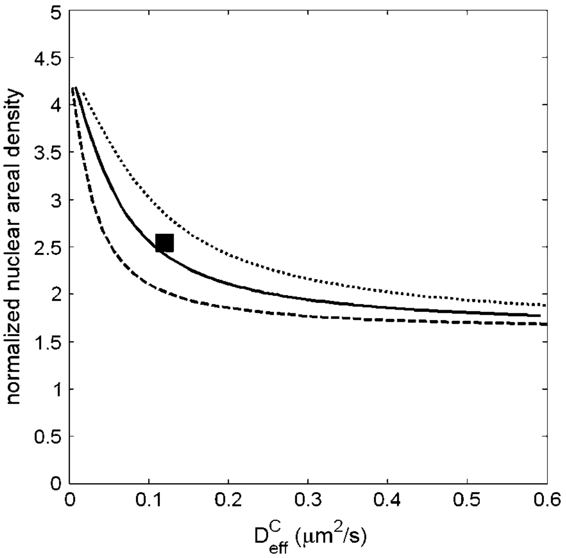

FIGURE 5 Normalized nuclear density at 90 min postinfection as a function of apparent transport coefficients, V^C_{eff} and D^C_{eff}; k^C and k'^C are adjusted to keep V^C_{eff} constant while varying D^C_{eff}. The dashed, solid, and dotted lines represent $V^C_{\mathrm{eff}} = -0.01\,\mu\mathrm{m/s}$, $-0.019\,\mu\mathrm{m/s}$, and $-0.03\mu\mathrm{m/s}$, respectively. The solid square represents experimental observations of Ad2 in HeLa cells ($V^C_{\mathrm{eff}} = -0.019\,\mu\mathrm{m/s}$ and $D^C_{\mathrm{eff}} = 0.12\,\mu\mathrm{m}^2/\mathrm{s}$).

density, in other words, availability of cytoskeletal tracks for directional transport.

Experimentally, one can alter the dynamics and organization of cellular microtubules by adding nocodazole, a microtubule-depolymerizing drug, to the extracellular solution. Various studies have reported that administration of nocodazole ($>0.1\ \mu$M) blocks nuclear transport of viruses and reduces viral transgene expression (17). However, it is not clear how nocodazole-induced inhibition of viral transfection depends on its dose.

Nocodazole forms inactive complexes with tubulin dimers, reducing the free tubulin concentration. When tubulin concentration drops below a critical threshold, MTs will disassemble (24). The presence of nocodazole increases the catastrophe frequency, f_{cat}, and reduces the number of stable MTs, N_{MT} (30). In Appendix C, we formulate equations that relate f_{cat} and N_{MT} to nocodazole concentration $[NOC]$. Combining these equations with Eq. B1, we can calculate the forward binding rates $k^S_{\pm}$ for different concentrations of nocodazole. We postulate further that nocodazole does not influence the physics of motor-cargo-microtubule interactions. Thus, $V^S_{\pm}$ and $k'^S_{\pm}$ are unaffected by nocodazole; $k^S_{\pm}$ decreases progressively with $[NOC]$ and leads to smaller value of f_- and f_+. In other words, fewer viruses participate in MT-dependent transport as nocodazole is added to the extracellular solution. Since V_{eff} is proportional to $f_{\pm}$ and D_{eff} is proportional to $f^3_{\pm}$, the overall efficiency of nuclear-directed transport is expected to reduce considerably.

The above approximation is used to analyze the effects of nocodazole on nuclear accumulation and gene expression of Ad5 in human lung carcinoma A549 cells. The fractions of actively transported particles, f_- and f_+, are adjusted to reproduce the measured intracellular distribution of Ad5s in the absence of nocodazole (9). This is due to a lack of microscopic information on how Ad5s move inside A549 cells. Then, we vary $k^S_{\pm}$ as a function of $[NOC]$, while keeping all other parameters unchanged. Fig. 6 *a* shows the model predictions of viral intracellular distribution at 75 min for a wide range of $[NOC]$. The simulation results capture the dose-dependent inhibitory effect of nocodazole. Evidently, high concentrations of nocodazole block transport from the distal area to the nucleus. Treatment of cells with 2 and 20 μM NOC resulted in 50 and 60% inhibition of nuclear targeting of incoming adenoviruses, respectively. The viral density in the nuclear region is only slightly increased in comparison to the initial value of 1.

Inhibition of microtubule-dependent transport reduces the amount of exogenous DNA delivered to the nucleus. To quantify this effect, we use the model to simulate experiments that measure β-Gal expression of Ad5s in A549 cells (9). The cells contain either intact or NOC-disrupted microtubules. The equations used to describe transcription/translation of the exogenous DNA were given in model formulation. The predicted and measured levels of gene expression at 7 h p.i. (normalized with control) are shown in Fig. 6 *b* as function of $[NOC]$. Small concentrations of NOC ($[NOC] < 0.4\ \mu$M) only partially destabilize the MT network and have only a slight effect on β-Gal expression. On the other hand, high concentrations of NOC ($[NOC] > 10\ \mu$M) completely depolymerize the microtubule network, preventing viral targeting to the nucleus. Only a few viruses initially located in the nuclear region are able to bind to the nuclear membrane and release the exogenous DNA into the nucleus. This severely reduces transgene expression to merely 10–20% compared to untreated cells. The model overpredicts β-Gal activity for $[NOC] = 20\ \mu$M, possibly due to overestimation of diffusive transport in the cytosol at high NOC concentration.

DISCUSSION

Pharmacokinetic model versus current approach

Previously published kinetic models provided a major boost to the field by providing a mathematical description of viral infection for the first time. The major shortcoming of kinetic models is their simplified treatment of spatial organization and transport processes. For instance, Dee et al. (11) and Dee and Shuler (12) used a simple first-order kinetic equation to describe transport of cytosolic viruses to the nucleus: $(dV_{\mathrm{N}}/dt) = k_{\mathrm{n}}V_{\mathrm{C}}$, where V_{C} and V_{N} are the number of viruses in the cytosol and in the nucleus. The nuclear transport rate, k_{n}, is a lumped representation of several processes, including MT-based trafficking, diffusion, and binding to and translocation through the nuclear envelope. The numerical value of k_{n} was obtained by fitting the model predictions to

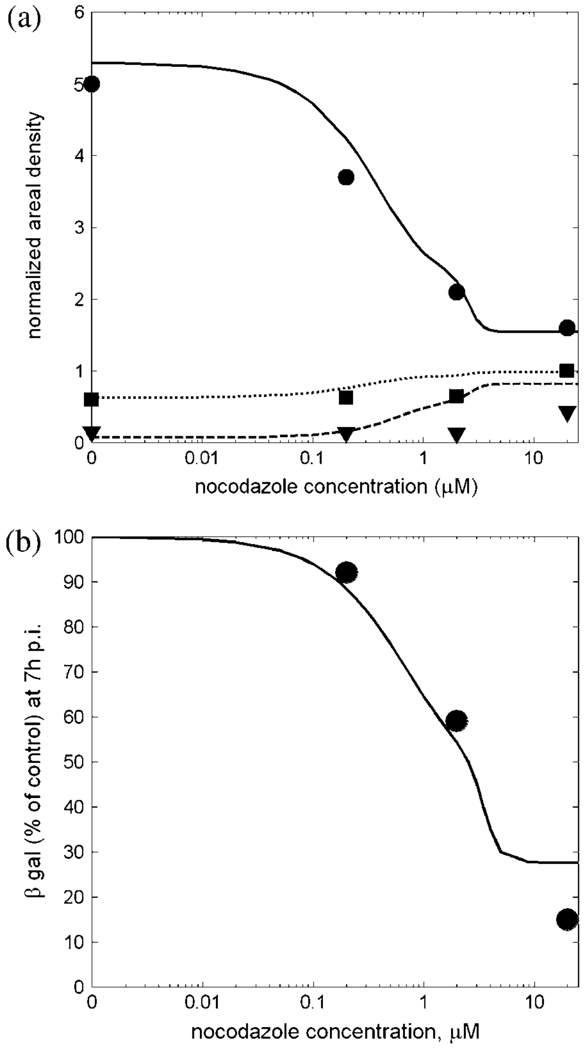

FIGURE 6 (*a*) Normalized areal density in different cellular regions at 75 min postinfection as a function of nocodazole concentration. Data was reproduced from Mabit (9) for intracellular distribution of Ad5 in A549 cells. The cellular regions are peripheral (*dashed line*, model; ▼, data), cytoplasmic (*dotted line*, model; ■, data), and perinuclear and nuclear (*solid line*, model; ●, data). (*b*) Viral gene expression at 7 h postinfection as a function of nocodazole concentration (*solid line*, model; ●, data). Data was reproduced from Mabit (9) for Ad5-mediated expression of β-gal in A549 cells.

experimental data. This approximation does not reflect the fact that the rate of nuclear entry depends on the local concentration of viruses bound to the nuclear envelope. Accordingly, k_{n} does not have a real physical meaning, rather it is adjusted to match the temporal evolution of V_{C} or V_{N}. Fitting of k_{n} to data also involves great uncertainties, sometimes up to ±50% (12). Because transport issues are not properly addressed in the kinetic approach, the use of k_{n} fails to reflect the effects of agents such as nocodazole, which reduce the local concentration of virus in the perinuclear region considerably, while V_{C} remains the same. This leads to overpredictions of nuclear localization and viral gene expression.

To overcome these issues, we introduced two new features in the present model. First, we introduced a continuous spatial coordinate to represent the cell geometry. So viral trafficking is represented as a continuous flow of particles rather than discrete jumps from one compartment to another. Second, we introduced transport coefficients (diffusion and convection) to describe viral dynamics wherever applicable.

This approach has several advantages. It enables us to develop a realistic and mechanistic description of microtubule-dependent transport. The viral particles are allowed to switch intermittently between diffusion and motor-driven directional movements on MTs just as they do in experiments. Although the model requires several more parameters to characterize binding and detachment of viruses to MTs, these parameters are real, have a physical meaning, and can be estimated directly from microscopic single-particle tracking experiments.

Thus, the present work is a step toward a more realistic description of intracellular transport in general. The model relates microscopic-scale microtubular binding and trafficking events ($l \sim 10^{-1}$ μm and $t \sim 10^{-1}$ s) to viral propagation at the whole-cell level ($l \sim 10^{1}$–10^{2} μm and $t \sim 10^{3}$–10^{4} s), and eventually to gene delivery efficiency. Furthermore, the description motivates a definition for the biophysical states of individual viral particles. Each viral state corresponds to a step in the infection pathway and possesses a distinct transport pattern. The mechanistic treatment of viral transport allows us to predict how viral trafficking depends on microtubule organization and dynamics, interactions between virus and motor proteins and spatial-heterogeneity. For instance, the model was used to predict, from first principles, how drugs such as nocodazole affect viral infection. The same approach can be used to analyze the effects of similar therapeutic agents such as colchicine, vinblastine, and taxol.

Characterization of MT-dependent trafficking

The model describes spatiotemporal evolution of viral distribution inside the cells. Upon internalization, viral particles are randomly distributed over the cell surface. Subsequent to endosomal escape, naked viruses in the cytosol are able to recruit motor proteins and travel on microtubules. Since free diffusion in the cytosol is slow, particles bound to an MT are unlikely to move far away from the MT after binding to it. Transport becomes more or less one-dimensional along the radial coordinate. The random walks in both directions on MTs define a form of biased facilitated diffusion with a drift velocity $V_{\mathrm{eff}}^{\mathrm{C}}$ and an effective diffusion coefficient $D_{\mathrm{eff}}^{\mathrm{C}}$ (13,31,32). $V_{\mathrm{eff}}^{\mathrm{C}}$ measures virus's bulk movement rate or the tendency of particles to move toward a particular direction, whereas $D_{\mathrm{eff}}^{\mathrm{C}}$ measures the total dispersal rate or the tendency of particles to move in both directions. Thus, $V_{\mathrm{eff}}^{\mathrm{C}}$ reflects the ability of particles to accumulate, whereas $D_{\mathrm{eff}}^{\mathrm{C}}$ reflects the ability of particles to equilibrate along MTs.

Consider a special case, $V_{\mathrm{eff}}^{\mathrm{C}} = 0$. Such unbiased bidirectional transport does not result in any net transport.

However, at short times, the radial density $n(r,t)$ is higher at the cell periphery, because of initial 2D random allocation of viruses (see Fig. 3 *a*). This leads to a nonequilibrium condition from a 1D perspective. Due to enhanced dispersion of particle movements, $n(r,t)$ will gradually equilibrate along the radial coordinate r. As a result, viral particles are transported from the cell periphery toward the nucleus to remove the initial gradients of $n(r)$. The rate of such equilibration process is measured by $D_{\mathrm{eff}}^{\mathrm{C}}$. The more mobile the particles are, the faster the equilibration process is. So even in the case of unbiased bidirectional transport ($V_{\mathrm{eff}}^{\mathrm{C}} \sim 0$), viruses can be efficiently delivered to the nuclear region due to the initial imbalance of viral concentration along the MTs. This is quite contrary to the conventional wisdom on intracellular transport.

To compare these two coexisting and interdependent apparent transport processes, we use Peclet number, defined as follows,

$$Pe = \frac{t_{\mathrm{diff}}}{t_{\mathrm{conv}}} = \frac{L^2/D_{\mathrm{eff}}}{L/V_{\mathrm{eff}}} = \frac{LV_{\mathrm{eff}}}{D_{\mathrm{eff}}}, \tag{9}$$

where L is the length scale characterizing the system (for viral transport, $L = R_{\mathrm{C}} - R_{\mathrm{N}}$). If $Pe \gg 1$, a large gradient in concentration exists and the system shows an ''accumulative'' behavior. If $Pe \ll 1$, the system is ''dispersive'' as facilitated diffusion dominates the transport. In Table 5, the effective transport parameters were estimated for different viruses. Evidently, viruses utilize different strategies to propagate within the cells. Herpes simplex virus (HSV) relies on fast, directed axonal-transport to spread in sensory neuron cells (the ratio of anterograde/retrograde is ~7:1) (5). Similarly, adenoviruses move preferentially toward the nucleus but facilitated diffusion also contributes considerably to transport. On the contrary, adeno-associated virus (AAV) relies mostly on cytosolic diffusion to navigate inside the cytoplasm, only 8% of viral particles display directional transport (2).

Implications for viral gene delivery

Are microtubules always needed to deliver viral DNA? The model demonstrates that MT-trafficking is critical to successful infection of Ad2. What about other viruses? It is known that small gene carriers such as vRNP can reach the nucleus by diffusion (33). Thus, cytosolic mobility of a virus may determine which transport mechanism is needed. The cytosolic diffusivity D_0 of a virus can be estimated as $D_0 \sim (kT/3\pi\mu d_{\mathrm{p}})$, with k being the Boltzmann constant, T temperature in Kelvin, μ the dynamic viscosity of the cytosol, and d_{p} the apparent diameter of viral particles (34). Having established this, we can now evaluate localization of viruses in the nuclear area as a function of its apparent diameter (Fig. 7 *a*). We consider two different cases: A), viruses that only diffuse in cytosol and B), viruses that utilize both diffusion and MT-transport. Small viruses ($d_{\mathrm{p}} < 30$ nm) exhibit strong nuclear localization in both cases. Larger viruses ($d_{\mathrm{p}} > 200$–300 nm), as expected, are immobile in the cytosol and display insignificant nuclear transport, unless MT-transport is involved. We conclude that MT-dependent trafficking is critical to delivery of viruses exceeding 50 nm in diameter, while small viruses such as AAV can rely mostly on diffusion to arrive at the nucleus.

TABLE 5 V_{eff} and D_{eff} for different gene delivery systems

Gene vector/cell	V_{eff} (μm/s)	D_{eff} (μm^2/s)	Pe	References
Ad2/HeLa	−0.019	0.12	2	(6)
Ad2/TC7	−0.072	0.30	3.6	(6)
HSV/sensory neurons	0.5-1	4–5	4–6	(5)
AAV/HeLa	−0.011	0.9–1.5	0.11–0.15	(2)

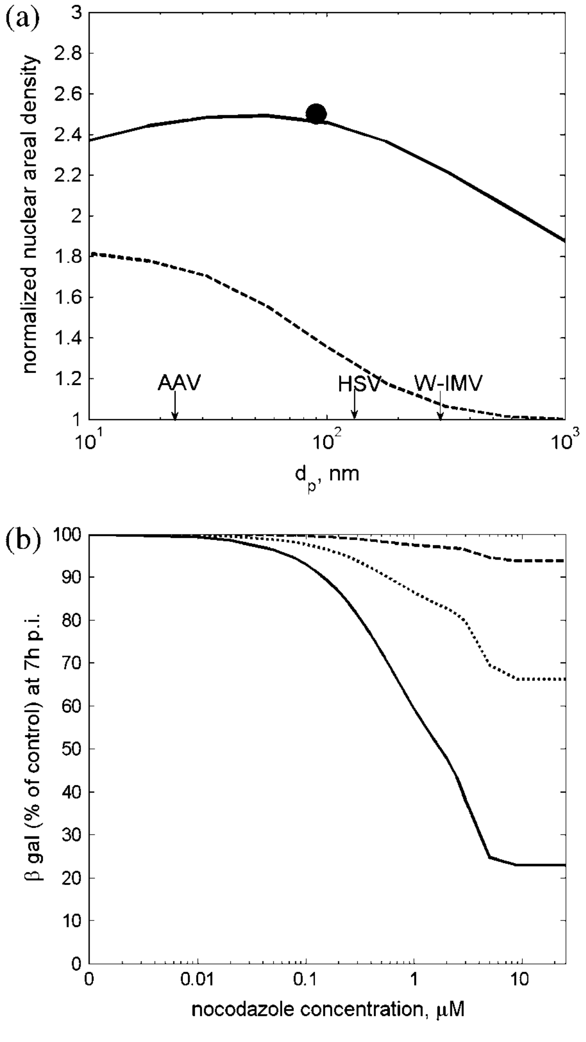

FIGURE 7 (*a*) Nuclear localization at 90 min postinfection as a function of the apparent diameter d_{p} of viruses that: 1), diffuse in cytosol (*dashed line*), and 2), utilize both diffusion and MT-transport (*solid line*). The circle represents experimental data obtained for Ad2 in HeLa cells. AAV, adeno-associated virus; HSV, herpes simplex virus; W-IMV, vaccinia virus. (*b*) Influence of the cell dimensions on viral gene expression. Ad2-mediated expression of β-gal activity at 7 h postinfection as a function of $R_{\mathrm{N}}/R_{\mathrm{C}}$ (*solid line*, $R_{\mathrm{N}}/R_{\mathrm{C}} = 0.25$; *dotted line*, $R_{\mathrm{N}}/R_{\mathrm{C}} = 0.5$; *dashed line*, $R_{\mathrm{N}}/R_{\mathrm{C}} = 0.75$). The nuclear radius is kept constant, $R_{\mathrm{N}} = 6$ μm.

Cell geometry might also influence how microtubule-mediated transport controls viral gene expression. In the present model, cell geometry is represented by cell radius, R_C and nuclear radius, R_N. The effects of cell dimension on viral gene delivery were examined by repeating the calculations with nocodazole for a variety of cell configurations (see Fig. 7 *b*). As R_N/R_C approaches 1, nocodazole no longer successfully inhibits viral gene expression. For $R_N = 0.75\ R_C$, β-gal activity at $[NOC] = 20\ \mu M$ is merely ~5% less than the control. Thus, the role of microtubule-based transport diminishes as the cell radius becomes comparable to the nuclear radius, because most of the internalized viruses are already in the nuclear region. This is consistent with experimental observations that cells that are particularly small will be infected in the absence of MTs if enough time is allowed (9).

Alternatively, viruses can take advantage of the host cell mechanism for transporting material from the cell periphery to the perinuclear region. For instance, Ad7 is retained inside the endosomes for a long time after entry and is subsequently delivered to lysosomes (35). Since lysosomes locate in the vicinity of the nucleus, a delayed escape from lysosomes facilitates nuclear localization of Ad7. In this case, MT-trafficking also plays a principal role in delivering the vesicle content from the endosomes to the lysosomes. The model can be modified (by introducing a biophysical state to represent the lysosomal viruses) to reflect the difference in intracellular routes of Ad7 and subgroup C Ads.

The above analysis is used to suggest improvements in designs of synthetic gene delivery systems. Synthetic gene vectors are created by condensing DNA molecules with cationic agents, such as cationic liposomes or cationic polymers (36). They are relatively large ($d \sim$ 150–400 nm) and do not possess the ability to recruit molecular motors and travel on MTs. Consequently, cytosolic transport has been identified as a critical barrier for synthetic gene delivery (36). In analogy to viral gene delivery, there are three different approaches to overcome this barrier. First, synthetic vectors can be condensed/packaged to smaller particles, allowing them to navigate easier within the cell. This also increases the probability of gene vectors getting through the nuclear pore complexes. However, highly condensed DNA complexes may prevent the DNA from efficiently unpacking and dissociating from the cationic agent. Second, the synthetic vectors can be conjugated with molecules that have high affinity for motor proteins. This will facilitate the recruitment of molecular motors for MT-transport. Third, the vectors can be engineered to target the lysosomal pathways for cytoplasmic release (35). The main issue would be the stability of the synthetic vectors in the lysosomal compartment. The current model provides a quantitative framework to evaluate and to optimize these delivery strategies.

Cells use several mechanisms to control the activities and interactions of molecular motors to regulate directional movements on microtubules (37). There is evidence that viruses are able to utilize these mechanisms to enhance their nuclear targeting. For instance, Suomalainen et al. (38) demonstrated that adenoviral infection stimulates two distinct signaling pathways that enhance the MT-dependent retrograde transport of viral capsids. Thus, a potential antiviral strategy is to develop therapeutic agents that inhibit or impair dynein-driven transport of viruses, for instance, by interfering with binding of cytoplasmic dyneins to viral capsids or suppressing signaling events that enhance retrograde movements. Calculations show that such strategy can be very effective and reduces up to 90% of viral gene expression (data not shown). Alternatively, one can promote stable association of viruses with the MTOC (39,40) or with other cellular organelles in the perinuclear region. This reduces the mobility of viruses in the perinuclear region and consequently decreases diffusional transport from the perinuclear area to the nuclear area. The model predicts that such approach might inhibit up to 50–60% of nuclear delivery (data not shown).

Modeling issues and uncertainty quantification

Apparently, the present modeling approach is a seemingly rough aproximation to reality; however, it succeeds in providing a consistent and quantitative description for viral gene delivery at the cellular level, and lays a broad foundation for further developments. Future experimental and theoretical studies are required to strengthen several assumptions employed in the model. A number of important issues have not been fully addressed and call for further examination, including the effects of sorting/recycling endosomes, capsid degradation, multiplicity of infection, noncircular cell geometry, cell dimensionality and polarity, cell variability, and spatial and temporal dependence of transport coefficients. Currently, the effects of uncoating are implicitly described by the transition rates between different biophysical states. It is of great importance to address this process mechanistically and explicitly in future studies.

Another concern involved in modeling complex and dynamic phenomena such as intracellular transport is quantification of uncertainty. There are several probable sources of uncertainties, including erroneous measurements, inconsistent data handling/averaging, inaccurate physical picture, and errors in numerical discretization and solution. All these sources of uncertainties must be accounted for when comparisons between experimental data and simulation output are used to make inferences about the model. In Appendix D, we develop a method to assess uncertainties in parameter estimation. We demonstrate that uncertainties in determination of detachment rate, k', and endosomal escape rate, k_{escape} lead to 20–30% errors in model predictions.

CONCLUSION

In this study, we have developed a comprehensive and integrative computational framework for intracellular trafficking and gene expression of adenoviruses. The numerical values of the model parameters were adapted directly from previous reports in literature. Without any fitting, the model was able to predict the measured spatiotemporal distribution of Ads in HeLa cells with a reasonable agreement. We used the model to quantify the role of microtubule-transport on nuclear targeting of viruses. Such quantitative understanding is important in developing therapeutic applications and antiviral strategies for adenovirus. With appropriate modifications, the modeling approach can be applied to other viruses, including human immunodeficiency virus and herpes simplex virus.

The real value of the model is in using transport processes (diffusion and convention) to describe important steps in viral transport. In doing so, the model makes a strong step toward realistic and physically based description of viral dynamics. As more and more mechanistic information become available on viral dynamics, such realistic models that are applicable for a broad set of data (beyond the data used for determining model parameters) will prove valuable.

APPENDIX A: ESTIMATION OF MODEL PARAMETERS

Cell geometry

The cell lines under consideration (HeLa and A549) are generally flat and can be approximated as two-dimensional planes. Cell dimensions are estimated from images shown in literature (9,16). The images were copied to and processed in Adobe Photoshop and the location of the cell membrane and the nuclear membrane were visually defined. The coordinates of points on these two boundaries were then determined manually from the pixel position. The cell center is defined as the mean of the horizontal and vertical coordinates of all points on the nuclear membrane. The nuclear radius, R_N, was calculated by averaging the distance from the nuclear membrane to the cell center. The cell radius, R_C, was obtained using the same procedure.

Transition rates

The transition rates between different infection stages are derived from previous kinetic studies of Ad5 and Ad2 trafficking and propagation in HeLa or A549 cells. The characteristic times (half-maximal) of internalization, endosomal escape, attachment to nuclear membrane, and capsid disassembly are 3–10 min (41), 10–20 min (42,43), 30–40 min (44), and 60–120 min (7,23), respectively. The corresponding transition rates are $k_{\mathrm{int}} = 1.2\ 10^{-3}$ s^{-1}, $k_{\mathrm{escape}} = 7.7\ 10^{-4}\ \mathrm{s}^{-1}$, $k_{\mathrm{nuclear}} = 4.8\ 10^{-4}\ \mathrm{s}^{-1}$, and $k_{\mathrm{disassembly}} = 1.3\ 10^{-4}\ \mathrm{s}^{-1}$. An important assumption is that these rates are independent of the number of viruses per cell, v_0.

Transport coefficients

The parameters that characterize transport properties of viral biophysical states are summarized in Table 3 for intracellular trafficking of Ad2 in HeLa cells. The parameters were adapted from particle-tracking data provided by Soulamainen et al. (6). The authors reported the average velocities V_+ and V_- of motor-assisted movements and the fractions of diffusive (f_0) and actively transported particles (f_- and f_+) for membrane-bound and cytosolic viruses. The duration of directional movements was observed to be ~2 s. This gives the detachment rate from MTs $k'_{\pm} \sim 0.5\ \mathrm{s}^{-1}$. f_- and f_+ are related to the binding rates $k_{\pm}$ by the following equations, obtained by integration of Eq.1 along r in the cytoplasmic region,

$$f_-^{\mathrm{S}} = \frac{v_-^{\mathrm{S}}}{v^{\mathrm{S}}} \cong \frac{\dfrac{k_-^{\mathrm{S}}}{k_-^{'\mathrm{S}}}}{1+\dfrac{k_-^{\mathrm{S}}}{k_-^{'\mathrm{S}}}+\dfrac{k_+^{\mathrm{S}}}{k_+^{'\mathrm{S}}}} \qquad \text{(A1)}$$

$$f_+^{\mathrm{S}} = \frac{v_+^{\mathrm{S}}}{v^{\mathrm{S}}} \cong \frac{\dfrac{k_+^{\mathrm{S}}}{k_+^{'\mathrm{S}}}}{1+\dfrac{k_-^{\mathrm{S}}}{k_-^{'\mathrm{S}}}+\dfrac{k_+^{\mathrm{S}}}{k_+^{'\mathrm{S}}}}. \qquad \text{(A2)}$$

For endosomal viruses, we postulate that their transport properties resemble those of Ts1 mutant adenoviruses, which are incapable of escaping from endosomes (6). Due to lack of information, the transport parameters of empty capsids are set to be equal to those of cytosolic viruses.

Gene expression

We focus on expression of *lacZ* gene, which encodes β-galactosidase enzyme, in mammalian cells. The kinetic parameters are adapted from a variety of sources. The transcription rate is a lumped representation of several biochemical and biophysical processes, including synthesis of mRNA from DNA template (10^3 transcripts per hour) and export of mRNA from nuclear to cytosol (2–3 h^{-1}) (15). The rate of β-galactoside production through mRNA translation is ~1.66 10^{-2} min^{-1} (45). The average half-life of mRNA in HeLa cells is ~5 h, which gives a degradation rate of 0.14 h^{-1} (46). The degradation rate of β-galactosidase is much slower, 0.05 h^{-1} (47).

APPENDIX B: RELATION BETWEEN MT DYNAMICS AND ORGANIZATION AND BINDING RATES TO MTS

Let's consider a viral particle in the neighborhood of an MT. Since free diffusion in cytoplasm is slow, particles once bound to MT are unlikely to move far away. This implies that viruses are likely to bind to MTs that they just detach from. Due to microtubule-motor-capsid interactions, it takes on average t_{bind} seconds for a viral particle to bind to and get carried on the MT. For adenoviruses, $t_{\mathrm{bind}} \sim 0.5$–1 s (6).

Because of dynamic instability, an MT may completely depolymerize before the virus has a chance to interact with it. The probability that an MT disappears before binding occurs is $(t_{\mathrm{bind}}/t_{1/2}^{\mathrm{MT}})$, where $t_{1/2}^{\mathrm{MT}}$ is the half-life of microtubules. A virus that unsuccessfully binds to a neighboring MT must search diffusively for another MT. The average time required for finding a new MT is $(\delta_{\mathrm{MT}}^2/D_0)$, where δ_{MT} is the average spacing between microtubules and D is the diffusion coefficient of viral particles in cytoplasm. Thus, the average interval between two directional transport (binding) events can be estimated as follows

$$t_{\mathrm{off}} = \frac{1}{k} \approx \left(1-\frac{t_{\mathrm{bind}}}{t_{1/2}^{\mathrm{MT}}}\right)t_{\mathrm{bind}} + \frac{t_{\mathrm{bind}}}{t_{1/2}^{\mathrm{MT}}}\left(t_{\mathrm{bind}}+\frac{\delta_{\mathrm{MT}}^2}{D_0}\right) = t_{\mathrm{bind}} + \frac{t_{\mathrm{bind}}^2}{t_{1/2}^{\mathrm{MT}}}\frac{\delta_{\mathrm{MT}}^2}{D_0}. \qquad \text{(B1)}$$

The second term in Eq. B1 depends on stability and availability of cytoskeletal tracks. As a first-order approximation, $t_{1/2}^{\mathrm{MT}} \sim \ln 2/f_{\mathrm{cat}}$ (f_{cat} is the rate of catastrophe) and $\delta_{\mathrm{MT}} \sim \pi(R_{\mathrm{N}} + R_{\mathrm{C}})/N_{\mathrm{MT}}$ (N_{MT} is the number of microtubules inside a cell). In general, $(t_{\mathrm{bind}}^2/t_{1/2}^{\mathrm{MT}})(\delta_{\mathrm{MT}}^2/D_0)$ is small compared to t_{bind} and $t_{\mathrm{off}} \sim t_{\mathrm{bind}}$. However, in the presence of microtubule-destabilizing drugs such as nocodazole, colchicines, and vinblastine, $(t_{\mathrm{bind}}^2/t_{1/2}^{\mathrm{MT}})(\delta_{\mathrm{MT}}^2/D_0)$ becomes significant as the availability and stability of MTs are reduced.

APPENDIX C: EFFECTS OF NOCODAZOLE ON MICROTUBULE ORGANIZATION AND DYNAMICS

Nocodazole forms inactive complexes with tubulin dimers, and reduces the concentration of tubulin available for microtubule polymerization, c_t. The simplest reaction mechanism for this process is (48,49)

$$T + N \leftrightarrow TN \leftrightarrow T^{*}N, \tag{C1}$$

where T and N represent tubulin dimers and nocodazole, respectively.

The steady-state concentration of tubulin after adding nocodazole to the extracellular solution can be expressed by Michaelis-Menten enzymatic kinetic (49) as

$$c_t = c_0 \frac{K_M}{K_M + [NOC]}, \tag{C2}$$

where c_0 is the total tubulin concentration, $[NOC]$ is the nocodazole concentration, and K_M is the Michaelis constant.

Previous theoretical studies (50,51) suppose that the catastrophe rate f_{cat} depends exponentially on c_t, $f_{cat} \sim exp(-c_t/c_f)$, where c_f is a decay constant. Several experimental studies confirmed this statement (52,53). From Eq. C2, we have

$$\frac{f_{cat}}{f^0_{cat}} = \exp\left(\frac{c_0}{c_f}\frac{[NOC]}{K_M + [NOC]}\right), \tag{C3}$$

where f^0_{cat} is the catastrophe frequency in the absence of $[NOC]$. Vasquez et al. (30) showed that for high concentration of $[NOC]$, (f_{cat}/f^0_{cat}) is ~3.5–4. This gives $(c_0/c_f) \sim 1.2–1.3$.

Caudron et al. (52) showed that the nucleation rate ν is proportional to $c_t^{6.2}$. Assuming that the number of microtubules N_{MT} is proportional to the nucleation rate, we have

$$\frac{N_{MT}}{N^0_{MT}} = \frac{\delta^0_{MT}}{\delta_{MT}} = \left(\frac{c_t}{c_0}\right)^{6.2} = \left(\frac{K_M}{K_M + [NOC]}\right)^{6.2}. \tag{C4}$$

$K_M = 2–3\ \mu M$ provides the best fit to data obtained by Mabit et al. (9). Equations C3 and C4 are only valid for $[NOC] > 0.05–0.1\ \mu M$. Lower concentrations of nocodazole, <10 nM, suppressed microtubule dynamics and enhanced MT-mediated trafficking of Ads (27). The underlying mechanism for such stabilizing effects is not completely understood and is not considered in this study.

APPENDIX D: UNCERTAINTY ANALYSIS

The model described in this article is deterministic, but the knowledge about some of the input parameters is uncertain. We develop a method to assess uncertainty in model predictions using Monte Carlo simulations, in which uncertainty of each input parameter is described by probability density function. The probability density functions are constructed based on literature reviews and expert opinions, similar to construction of Bayesian prior distributions (54). Once the probability density functions are defined for all parameters, a complete set of input parameters is sampled from them and fed into the model, producing a realized spatiotemporal pattern of viruses. This process is repeated 1000 times, resulting in 1000 realizations of intracellular allocation of viruses. The sampled viral distributions are analyzed and compared with experimental data.

Because the number of parameters involved in this model is quite large, the proposed procedure requires extensive computational resources. For demonstration purpose, we choose to analyze error propagation of the detachment rate from MTs, k', and the endosomal escape rate, k_{escape}. These two parameters are believed to have great impacts on model predictions. Based on previous data (6,42), the ranges of k' and k_{escape} are estimated to be 0.33–2 s^{-1} and 4.6 10^{-4}–2.3 10^{-3} s^{-1}, respectively. Due to lack of information, we assume a uniform probability density function for both parameters. Other model parameters are kept the same as in Tables 3 and 4.

TABLE 6 Results of Monte Carlo simulations: normalized nuclear density of Ad2 in HeLa cells at $t = 30$, 60, and 90 min p.i.

Time	Data	Mean	Min	Max	± SD
30 min p.i.	1.6	1.45	1.15	2.21	0.21
60 min p.i.	2.3	2.18	1.54	3.25	0.34
90 min p.i.	2.5	2.56	1.97	3.68	0.35

Data was reproduced from Nakano and Greber (16).

Results of Monte Carlo simulations are summarized in Table 6. Large intervals of predicted nuclear density are observed for $t = 30$, 60, and 90 min. On the other hand, the means are comparable to experimental data (16) and the standard deviations are only 10–15% of the means. Clearly, we still need to conduct more experiments to obtain better estimates of k', and k_{escape}. Nevertheless, the model is sufficiently robust such as large errors in k' and k_{escape} do not lead to unphysical predictions.

We thank Prof. Nam Dinh and Chinmay Pangarkar for their helpful discussions related to the subject. Special thanks to Prof. Urs F. Greber for answering questions related to experimental observations.

A. T. Dinh is supported by the University of California Biotech Fellowship Program.

REFERENCES

1. Verma, I. M., and N. Somia. 1997. Gene therapy: promises, problems and prospects. *Nature.* 389:239–242.
2. Seisenberger, G., M. U. Ried, T. Endress, H. Buning, M. Hallek, and S. Brauchle. 2001. Real-time single-molecule imaging of the infection pathway of an adeno-associated virus. *Science.* 294:1929–1932.
3. Lakadamyali, M., M. J. Rust, H. P. Babcock, and X. W. Zhuang. 2003. Visualizing infection of individual influenza viruses. *Proc. Natl. Acad. Sci. USA.* 100:9280–9285.
4. McDonald, D., M. A. Vodicka, G. Lucero, T. M. Svitkina, G. G. Borisy, M. Emerman, and T. J. Hope. 2002. Visualization of the intracellular behavior of HIV in living cells. *J. Cell Biol.* 159:441–452.
5. Smith, G. A., S. Gross, and L. W. Enquist. 2001. Herpesviruses use bidirectional fast-axonal transport to spread in sensory neurons. *Proc. Natl. Acad. Sci. USA.* 98:3466–3470.
6. Suomalainen, M., M. Y. Nakano, S. Keller, K. Boucke, R. P. Stidwill, and U. F. Geber. 1999. Microtubule-dependent plus- and minus-end-directed motilities are competing processes for nuclear targeting of adenovirus. *J. Cell Biol.* 144:657–672.
7. Greber, U. F., M. Willetts, P. Webster, and A. Helenius. 1993. Stepwise dismantling of adenovirus 2 during entry into cells. *Cell.* 75:477–486.
8. Kelkar, S. A., K. K. Pfister, R. G. Crystal, and P. L. Leopold. 2004. Cytoplasmic denyin mediates adenovirus binding to microtubules. *J. Virol.* 78:10122–10132.
9. Mabit, H., M. Y. Nakano, U. Prank, B. Saam, K. Dohner, B. Sodeik, and U. F. Greber. 2002. Intact microtubules support adenovirus and herpes simplex virus infections. *J. Virol.* 76:9962–9971.
10. Ledley, F. D., and T. S. Ledley. 1998. Pharmacokinetic considerations in somatic gene therapy. *Adv. Drug Deliv. Rev.* 30:133–150.
11. Dee, K. U., D. A. Hammer, and M. L. Shuler. 1995. A model of the binding, entry, uncoating, and RNA synthesis of Semliki Forest virus in baby hamster kidney (BHK-21) cells. *Biotechnol. Bioeng.* 46: 485–496.

12. Dee, K. U., and M. L. Shuler. 1997. A mathematical model of the trafficking of acid-dependent enveloped viruses: application to the binding, uptake, and nuclear accumulation of baculovirus. *Biotechnol. Bioeng*. 54:468–490.
13. Smith, D. A., and R. M. Simmons. 2001. Models of motor-assisted transport of intracellular particles. *Biophys. J.* 80:45–68.
14. Kamiya, H., H. Akita, and H. Harashima. 2003. Pharmacokinetic and pharmacodynamic considerations in gene therapy. *Drug Discov. Today*. 8:990–996.
15. Reddy, B., and J. Yin. 1999. Quantitative intracellular kinetics of HIV-1. *AIDS Res. Hum. Retroviruses*. 15:273–283.
16. Nakano, M. Y., and U. F. Greber. 2000. Quantitative microscopy of fluorescence adenovirus entry. *J. Struct. Biol.* 129:57–68.
17. Meier, O., and U. F. Greber. 2003. Adenovirus endocytosis. *J. Gene Med*. 5:451–462.
18. Kovesdi, I., D. E. Brough, J. T. Bruder, and T. J. Wickham. 1997. Adenoviral vectors for gene transfer. *Curr. Opin. Biotechnol.* 8:583–589.
19. Murray, J. W., E. Bananis, and A. W. Wolkoff. 2000. Reconstitution of ATP-dependent movement of endocytic vesicles along microtubules in vitro: an oscillatory bidirectional process. *Mol. Biol. Cell*. 11:419–433.
20. Murray, J. W., and A. W. Wolkoff. 2003. Roles of the cytoskeleton and motor proteins in endocytic sorting. *Adv. Drug Deliv. Rev.* 55:1385–1403.
21. Nielsen, E., F. Severin, J. M. Backer, A. Hyman, and M. Zerial. 1999. Rab5 regulates motility of early endosomes on microtubules. *Nat. Cell Biol.* 1:376–382.
22. Whittaker, G. R., M. Kann, and A. Helenius. 2003. Viral entry into the nucleus. *Annu. Rev. Cell Dev. Biol.* 16:627–651.
23. Trotman, L., N. Mosberger, M. Fornerod, R. P. Stidwill, and U. F. Greber. 2001. Import of adenovirus DNA involves the nuclear pore complex receptor CAN/Nup214 and histone H1. *Nat. Cell Biol.* 3:1092–1100.
24. Desai, A., and T. J. Mitchison. 1997. Microtubule polymerization dynamics. *Annu. Rev. Cell Dev. Biol.* 13:83–117.
25. Mandelkow, E., and E. M. Madelkow. 1995. Microtubules and microtubule-associated proteins. *Curr. Opin. Cell Biol.* 7:72–81.
26. Schliwa, M., and G. Woehlke. 2003. Molecular motors. *Nature*. 422:759–765.
27. Giannakakou, P., M. Nakano, K. C. Nicolaou, A. O'Brate, J. Yu, M. V. Blagosklonny, U. F. Greber, and T. Fojo. 2002. Enhanced microtubule-dependent trafficking and p53 nuclear accumulation by suppression of microtubule dynamics. *Proc. Natl. Acad. Sci. USA*. 99:10855–10860.
28. Rodionov, V., J. Yi, A. Kashina, A. Oladipo, and S. P. Gross. 2003. Switching between microtubule- and actin-based transport systems in melanophores is controlled by cAMP levels. *Curr. Biol.* 13:1837–1847.
29. Sodeik, B., M. W. Ebersold, and A. Helenius. 1997. Microtubule-mediated transport of incoming herpes simplex virus 1 capsids to the nucleus. *J. Cell Biol.* 136:1007–1021.
30. Vasquez, R. J., B. Howell, A. M. Yvon, P. Wadsworth, and L. Cassimeris. 1997. Nanomolar concentrations of nocodazole alter microtubule dynamic instability in vivo and in vitro. *Mol. Biol. Cell*. 6:973–985.
31. Maly, I. V. 2002. A stochastic model for patterning of the cytoplasm by the saltatory movement. *J. Theor. Biol.* 216:59–71.
32. Grünbaum, D. 2000. Advection-diffusion equations for internal state-mediated random walks. *SIAM J. Appl. Math.* 61:43–73.
33. Babcock, H. P., C. Chen, and X. Zhuang. 2004. Using single-particle tracking to study nuclear trafficking of viral genes. *Biophys. J.* 87:2749–2758.
34. Sodeik, B. 2000. Mechanisms of viral transport in the cytoplasm. *Trends Microbiol*. 8:465–472.
35. Miyazawa, N., R. G. Crystal, and P. L. Leopold. 2001. Adenovirus serotype 7 retention in a late endosomal compartment prior to cytosol escape is modulated by fiber protein. *J. Virol.* 75:1387–1400.
36. Wiethoff, C. M., and C. R. Middaugh. 2003. Barriers to nonviral gene delivery. *J. Pharm. Sci.* 92:203–217.
37. Gross, S. P., M. A. Welte, S. M. Block, and E. F. Wieschaus. 2002. Coordination of opposite polarity microtubule motors. *J. Cell Biol.* 156:715–724.
38. Suomalainen, M., M. Y. Nakano, K. Boucke, R. P. Stidwill, and U. F. Geber. 2001. Adenovirus activated PKA and p38/MAPK pathways boost microtubule-mediated nuclear targeting of virus. *EMBO J.* 20:1310–1319.
39. Bailey, C. J., R. G. Crystal, and P. L. Leopold. 2003. Association of adenovirus with the microtubule organizing center. *J. Virol.* 77:13275–13287.
40. Strunze, S., L. C. Trotman, K. Boucke, and U. F. Greber. 2005. Nuclear targeting of adenovirus type 2 requires CRM1-mediated nuclear export. *Mol. Biol. Cell*. 16:2999–3009.
41. Leopold, P. L., B. Ferris, I. Grinberg, S. Worgall, N. R. Hackett, and R. G. Crystal. 1998. Fluorescent virions: dynamic tracking of the pathway of adenoviral gene transfer vectors in living cells. *Hum. Gene Ther.* 9:367–378.
42. Blumenthal, R., P. Seth, M. C. Willingham, and I. Pastan. 1986. pH-dependent lysis of liposomes by adenovirus. *Biochemistry*. 25:2231–2237.
43. Prchla, E., C. Plank, E. Wagner, D. Blaas, and R. Fuchs. 1995. Virus-mediated release of endosomal content in vitro: different behavior of adenovirus and rhinovirus serotype 2. *J. Cell Biol.* 131:111–123.
44. Wisnivesky, J. P., P. L. Leopold, and R. G. Crystal. 1999. Specific binding of the adenovirus capsid to the nuclear envelope. *Hum. Gene Ther.* 10:2187–2195.
45. Yildirim, N., and M. C. Mackey. 2003. Feedback regulation in the lactose operon: a mathematical modeling study and comparison with experimental data. *Biophys. J.* 84:2841–2851.
46. Jackson, D. A., A. Pombo, and F. Iborra. 2000. The balance sheet for transcription: an analysis of nuclear RNA metabolism in mammalian cells. *FASEB J.* 14:242–254.
47. Bachmair, A., D. Finley, and A. Varshavsky. 1986. In vivo half-life of a protein is a function of its amino-terminal residue. *Science*. 234:179–186.
48. Head, J., L. L. Y. Lee, D. J. Field, and J. C. Lee. 1985. Equilibrium and rapid kinetic studies on nocodazole-tubulin interaction. *J. Biol. Chem.* 260:11060–11066.
49. Xu, K., P. M. Schwarz, and R. F. Luduena. 2002. Interaction of nocodazole with tubulin isotypes. *Drug Dev. Res.* 55:91–96.
50. Marx, A., and E. Mandelkow. 1994. A model of microtubule oscillations. *Eur. Biophys. J.* 22:405–421.
51. Hammele, M., and W. Zimmermann. 2003. Modeling oscillatory microtubule polymerization. *Phys. Rev. E*. 67:021903.
52. Caudron, N., O. Valiron, Y. Usson, P. Valiron, and D. Job. 2000. A reassessment of the factors affecting microtubule assembly and disassembly in vitro. *J. Mol. Biol.* 297:211–220.
53. Pedigo, S., and R. C. Williams, Jr. 2002. Concentration dependence of variability in growth rates of microtubules. *Biophys. J.* 83:1809–1819.
54. Glimm, J., and D. H. Sharp. 1999. Prediction and the quantification of uncertainty. *Physica D*. 133:152–170.